

Characterization and Corrosion Behavior of High-Nitrogen HP-13Cr Stainless Steel in CO₂ and H₂S Environment

Bin Liu^{1,2,3,*}, Haiyang Zhao¹, Fang Li¹, Yujie Guo¹, Jiangjiang Zhang¹,
Wenguang Zeng¹, Lantian Yang¹, Haiou Sun²

¹ Key Laboratory of Enhanced Oil Recovery in Carbonate Fractured-vuggy Reservoirs, CNPC, and SINOPEC Northwest Company of China Petroleum and Chemical Corporation, Urumqi, Xinjiang, 831000, China.

² College of Power and Energy Engineering, Harbin Engineering University, Nantong ST 145, Harbin 150001, China.

³ Corrosion and Protection Laboratory, Key Laboratory of Superlight Materials and Surface Technology, Harbin Engineering University, Ministry of Education, Nantong ST 145, Harbin 150001, China.

*E-mail: liubin@hrbeu.edu.cn

Received: 6 September 2020 / Accepted: 17 October 2020 / Published: 30 November 2020

The effect of nitriding on the corrosive properties of HP-13Cr stainless steel in extremely aggressive environmental conditions was investigated. The composition, structure, and corrosion resistance of HP-13Cr before and after adding nitrogen were investigated with X-ray diffraction (XRD) analysis, X-ray photoelectron spectroscopy (XPS), atom probe tomography (APT), and electrochemical autoclave. The results show that nitrogen is probably enriched at the grain boundary during diffusion, strengthening the grain boundary. This plays a decisive role in the improvement of corrosion resistance. After nitriding, the corrosion resistance of HP-13Cr stainless steel in both CO₂ and CO₂/H₂S environments was significantly improved. This study provides a reference for this method to improve the corrosion resistance of stainless steel in extreme aggressive environments.

Keywords: stainless steel, pitting corrosion, nitriding, XPS

1. INTRODUCTION

During the development of oil and gas exploration, the existence of CO₂ and H₂S acidic gases will lead to severe corrosion of pipes. At present, the HP-13Cr stainless steel (SS) has been successfully applied in oil and gas application owing to good CO₂ corrosion resistance, mechanical properties, and low production costs compared with carbon steels and duplex SS grades [1,2]. However, super 13Cr SS requires CO₂ and a small amount of H₂S (0.001-0.003 MPa) environment

based on the detailed material selection guidelines in NACE MR0175/ISO 15156 [3,4]. Moreover, H₂S significantly affects stainless steel by accelerating the anodic dissolution reactions and cathodic process, resulting in severe weight loss and pitting corrosion. Hence, oil pipelines with higher corrosion resistance and lower production cost should be developed for CO₂ and H₂S environment.

Generally, alloying is an effective method to improve anticorrosion property by adding Mo, W, and N. Among them, N, an important alloying and inexpensive element, significantly enhanced the mechanical properties and corrosion resistance of stainless steel [5]. Addition of N is beneficial for decreasing the point defect density, promoting the Cr enrichment, and thickening the passive film. Yang et al. prepared a multilayer passivation film of a compound formed by nitrogen and chromium by cathodic arc evaporation [6]. Recently, Feng et al. reported an optimum nitrogen content of about 0.41 wt% for 30Cr15Mo1N steel manufactured by pressurized metallurgy. Additionally, ammonia or ammonium ions can react with free chlorine to inhibit the pitting corrosion of stainless steel. However, the low solubility of nitrogen in the martensitic stainless steel is a crucial factor restricting its development at atmospheric pressure. However, the corrosion resistance of nitriding stainless steel in extreme aggressive environment is still not studied in two aspects:

- (1) High temperature and high pressure environment has not been designed.
- (2) It is difficult to add nitrogen into martensitic stainless steel.

Therefore, we used HP-13Cr stainless steel prepared by a previously studied nitriding process, designed a simulation of high temperature and high pressure conditions of pipeline in an extreme environment, and compared the corrosion resistance of HP-13Cr stainless steel before and after nitriding.

2. EXPERIMENTAL PROCEDURE

2.1 Preparation of materials

HP-13Cr (N) SS was smelted under high nitrogen pressure. The smelting, homogenization, hot forging, and spheroidizing annealing processes are described in the previous study [20]. The chemical compositions of high nitrogen HP-13Cr SS and HP-13Cr SS are shown in Table 1. Specimens of 10 mm×10 mm×5 mm were cut from the plates, and the test surface was parallel to the forging direction. Then, the specimens were austenitized at 1020 °C for 40 min followed by quenching in oil, cryogenically treated at -80 °C for 2 h, and finally tempered twice at 300 °C for 2 h.

Table 1. Compositions (wt%) of HP-13Cr stainless steel and high nitrogen HP-13Cr stainless steel.

elements	C	Si	Mn	Cr	Mo	Ni	P	V	Cu	N	Al	Fe
HP-13Cr SS	0.03	0.15	0.51	12.77	2.19	5.36	0.02	0.014	0.047	0.002	0.037	balance
HP-13Cr(N)SS	0.03	0.15	0.51	12.77	2.19	5.36	0.02	0.014	0.047	0.3	0.037	balance

2.2. Microstructure characterization

The specimens were wet ground and polished with 1.5 μm diamond powder and then dried in cool air. To observe the grain size, the specimens were etched in a solution containing 3 g KMnO_4 , 6 mL H_2SO_4 , and 94 mL H_2O , and then observed using a DSX510 optical microscope (OM). To reveal the existing form of nitrogen, atomic-scale chemical analysis of HP-13Cr (N) was carried out using a CAMECA Instruments LEAP 4000 XHR. To prepare the specimens for atom probe tomography (APT) analysis, square rods with dimensions of 0.5 mm \times 0.5 mm \times 15 mm were cut from HP-13Cr (N) SS and then ground with 400 grit SiC paper until the cross-section reached about 0.4 mm \times 0.4 mm. Then, the needle-shaped specimens were electropolished using a standard two-step technique to ensure that the tip radius is less than 100 nm. The APT analysis was performed under an ultrahigh vacuum of $\sim 1 \times 10^{-8}$ Pa at a tip temperature of 50 K. The range of DC voltage was 3.0-4.4 kV, and the laser energy was 60 pJ. Finally, data reconstruction was carried out using Imago Visualization and Analysis Software (IVAS), version 3.6.8. X-ray diffraction (XRD) analysis was performed using a Rigaku SmartLab 9 kW X-ray diffractometer with Cu $\text{K}\alpha$ radiation at 45 kV, 200 mA, and 10°/min from 20° to 90°.

2.3 Specimens and solution

First, 50 mm \times 10 mm \times 3 mm specimens, including HP-13Cr SS and HP-13Cr (N) SS, were cut out from plates. Prior to testing, the specimen surface was ground using silicon carbide (SiC) paper to 2000 grit and then polished with 2.5 μm diamond to eliminate noticeable scratches and achieve a mirror finish surface. The simulation formation water was prepared using analytical-grade reagents and distilled water.

2.4 Immersion test

Immersion tests were carried out in a 5 L autoclave to evaluate the corrosion rate and corrosion morphology of HP-13Cr SS and HP-13Cr (N) SS in CO_2 (1.48 MPa) environment and CO_2 (1.48 MPa)/ H_2S (0.03 MPa) environment, respectively. Prior to each corrosion experiment, the formation water was deoxygenated with N_2 bubbling for 4 h. Then, 3.5 L formation water was introduced into the autoclave, sealed, and continuously bubbled with CO_2 at ambient temperature and pressure for 2 h to remove the oxygen present in the autoclave. Subsequently, the autoclave was heated to 70 °C, and a mixture of CO_2 and H_2S - CO_2 was introduced to the target pressure. After immersion test, the autoclave was cooled down to room temperature, and pressure was slowly released through a 12% NaOH scrubber. Nitrogen was purged through the regulator and autoclave to clean the residual H_2S overnight. After the immersion experiment, the specimens were taken out and rinsed with deionized water and anhydrous ethanol. Three specimens were descaled in a solution consisting of nitric acid (100 mL, density 1.42 g/mL), hydrofluoric acid (20 mL, density 1.15 g/mL), and deionized water (880 mL) at room temperature based on ASTM standard G1-03 [29] to remove the corrosion scale, and then

reweighed to obtain the final weight (W_1). The average corrosion rate (V_c) was reported in mm/a according to the obtained weight loss as follows:

$$V_c = \frac{87600(W_0 - W_1)}{t\rho A} \quad (1)$$

where W_0 is the original weight; t is the immersion time in h; ρ is the steel density in g/cm^3 ; A is the exposed surface area in cm^2 . Additionally, pitting corrosion was measured using a Zeiss confocal laser scanning microscope (OLS4100).

2.5 Electrochemical testing

The electrochemical measurements under CO_2 corrosion environment were performed using a high-temperature high- CO_2 pressure electrochemical autoclave and VersaSTAT 3F potentiostat/galvanostat. The electrochemical tests were performed in a conventional three-electrode cell equipped with a working electrode, a platinum counter electrode, and an external pressure balanced Ag/AgCl reference electrode. The electrodes were purchased from TOSHIN, UHP, Japan. The reference electrode was housed in a separate compartment under ambient temperature and pressure via a solution bridge. The reference solution was 0.1 M KCl. The electrode potentials were converted to standard hydrogen electrode (SHE) potential using the following relationship [30-32].

$$E_{\text{SHE}} = E_{\text{obs}} + 0.2866 - 0.001(T - T_0) + 1.754 \times 10^{-7}(T - T_0)^2 - 3.03 \times 10^{-9}(T - T_0)^3 \quad (2)$$

where E_{SHE} is the electrode potential vs. SHE; E_{obs} is the measured electrode potential vs. the Ag/AgCl reference electrode; T is the experimental temperature; T_0 is the room temperature (25 °C). Moreover, the electrochemical testing specimens were welded on 316L stainless steel alloy wires. To diminish the occurrence of galvanic corrosion, the welded point and stainless steel wires were subsequently shielded with silicone rubber (705). In addition, the specimens were potentiostatically polarized at $-1.3 V_{\text{SHE}}$ for 3 min to remove the surface oxide layer. Polarization curves were recorded from -300 mV with respect to the open circuit potential until the current density reached $1 \text{ mA}\cdot\text{cm}^{-2}$ at a constant scanning rate of $0.333 \text{ mV}\cdot\text{s}^{-1}$.

2.6 Characterization of scale film

The corrosion morphologies of HP-13Cr SS and HP-13Cr (N) SS under CO_2 and $\text{CO}_2/\text{H}_2\text{S}$ corrosion environment were analyzed using a field-emission scanning electron microscope (FE-SEM). X-ray photoelectron spectroscopy (XPS) was carried out using an ESCALAB250 instrument to analyze the corrosion scale of HP-13Cr SS and HP-13Cr (N) SS under CO_2 and $\text{CO}_2/\text{H}_2\text{S}$ corrosion environment. The high-resolution spectra were analyzed using XPSPEAK 4.0 software together with a database [28]; all the spectra were corrected to the carbon C 1s peak (284.6 eV).

3. RESULTS AND DISCUSSION

3.1 Microstructure

The optical microstructures of HP-13Cr SS and HP-13Cr (N) SS are shown in Figs. 1 (a) and (b), respectively. As shown in Figs. 1 (a) and (b), the microstructure of HP-13Cr SS and HP-13Cr (N) SS specimens are lath martensite and austenite phase, respectively. The grain size variation is considerably refined when 0.28N was added to the HP-13Cr SS. Similarly, in austenitic stainless steel, the addition of nitrogen can also improve the grain size [8]. As shown in Fig. 1 (c), both martensitic and austenitic peaks were observed for HP-13Cr SS and HP-13Cr (N) SS specimens. Fig. 1 (d) shows a three-dimensional (3D) atom by the atom tomographic reconstruction of HP-13Cr (N) SS. The Cr and N elements were distributed almost uniformly, and the N in HP-13Cr (N) SS exists in the form of solid solution state. This shows that nitrogen is probably enriched at the grain boundary during diffusion, strengthening the grain boundary. This plays a decisive role in the high corrosion resistance.

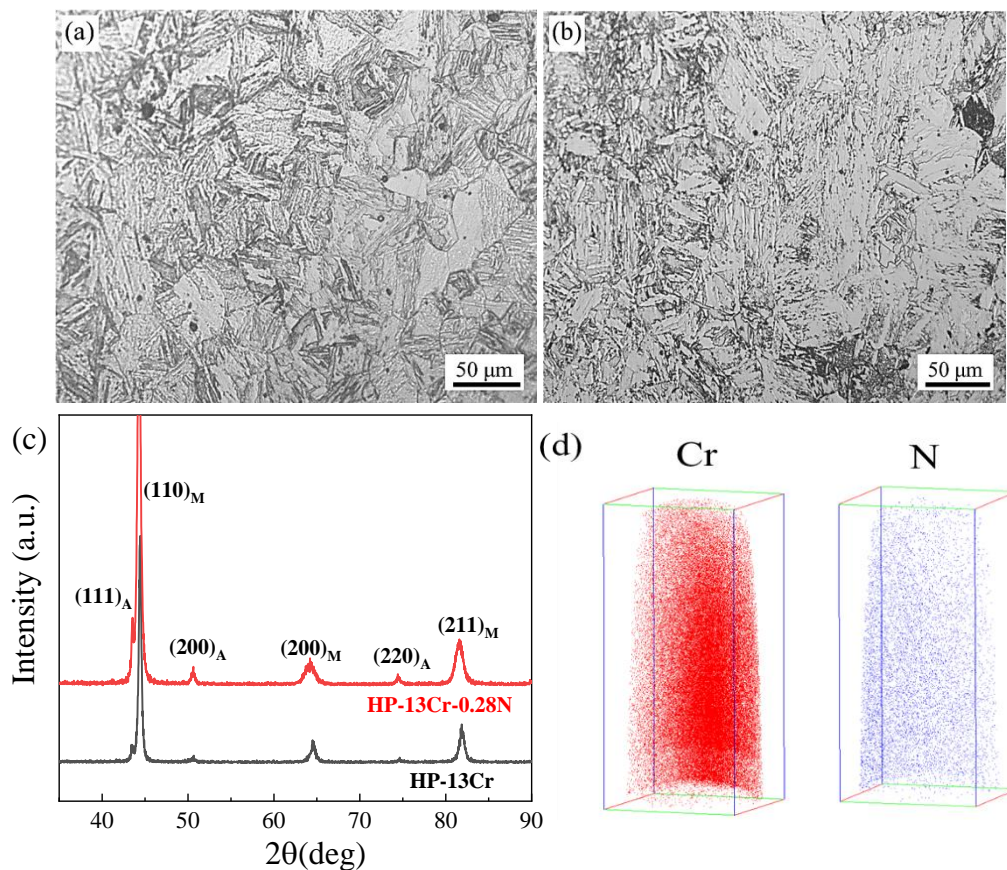


Figure 1. OM micrographs of (a) HP-13Cr SS and (b) HP-13Cr (N) SS. (c) XRD patterns of HP-13Cr SS and HP-13Cr (N) SS. (d) 3D atom by atom tomographic reconstruction of HP-13Cr (N) SS.

3.2 Corrosion macromorphology and corrosion rate

Fig. 2 shows the macroscopic images for HP-13Cr SS and HP-13Cr (N) SS before and after cleaning the corrosion scales at CO₂ and CO₂/H₂S corrosion environment, respectively. All the

samples at CO₂ corrosion environment look the same, and no corrosion products were observed on the surfaces. After the removal of corrosion scales, the macromorphology observation showed no obvious difference among the surfaces. However, both HP-13Cr and HP-13Cr(N) are partly covered with brown corrosion products at CO₂/H₂S corrosion environment. According to Li's report [12], the brown color of the corrosion products is due to the production of iron oxides. After removing the corrosion products, the surface of HP-13Cr becomes gray, while the surface of HP-13Cr(N) is brighter than HP-13Cr.

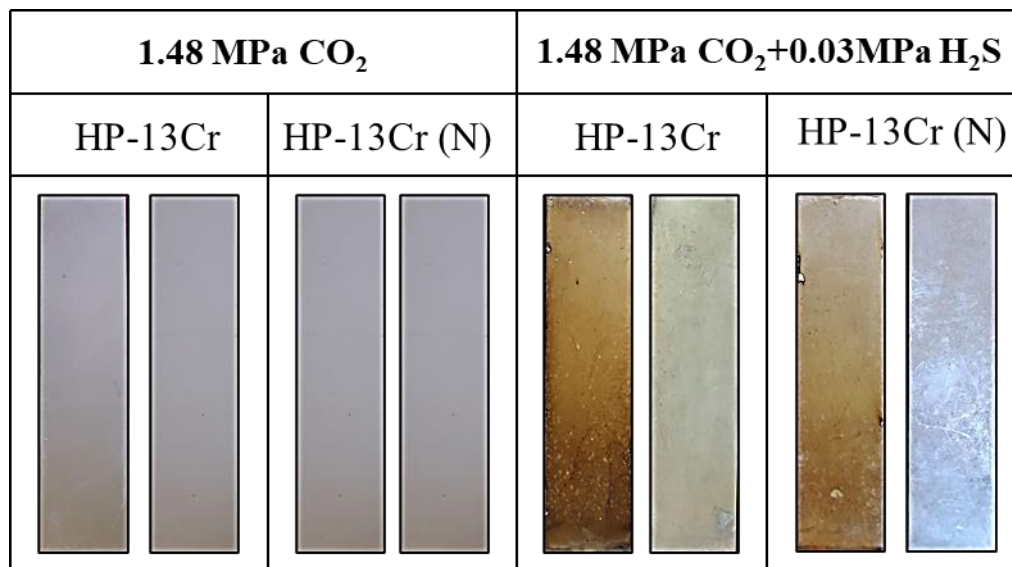


Figure 2. Macroscopic morphologies of HP-13Cr SS and HP-13Cr (N) and the morphology obtained after removing the corrosion scales at CO₂ (1.48 MPa) and CO₂ (1.48 MPa)/H₂S (0.03 MPa) and 70 °C corrosion environment.

Fig. 3 shows the average corrosion rate of HP-13Cr SS and HP-13Cr (N) SS obtained from CO₂ and CO₂/H₂S corrosion environment. After adding N, the corrosion rate of HP-13Cr stainless steel in CO₂ decreased from 1.0×10^{-3} mm/a to about 6×10^{-4} mm/a, a drop of 40%. In the CO₂/H₂S environment, the corrosion rate of nitrated stainless steel decreased from 2.0×10^{-3} mm/a to 8×10^{-4} mm/a compared to the base steel, a 60% reduction. The addition of nitrogen decreased the corrosion rate at two corrosion environments, especially in CO₂/H₂S corrosion environment. This indicates that N plays an important role in enhancing the corrosion resistance, which is consistent with previous research [33].

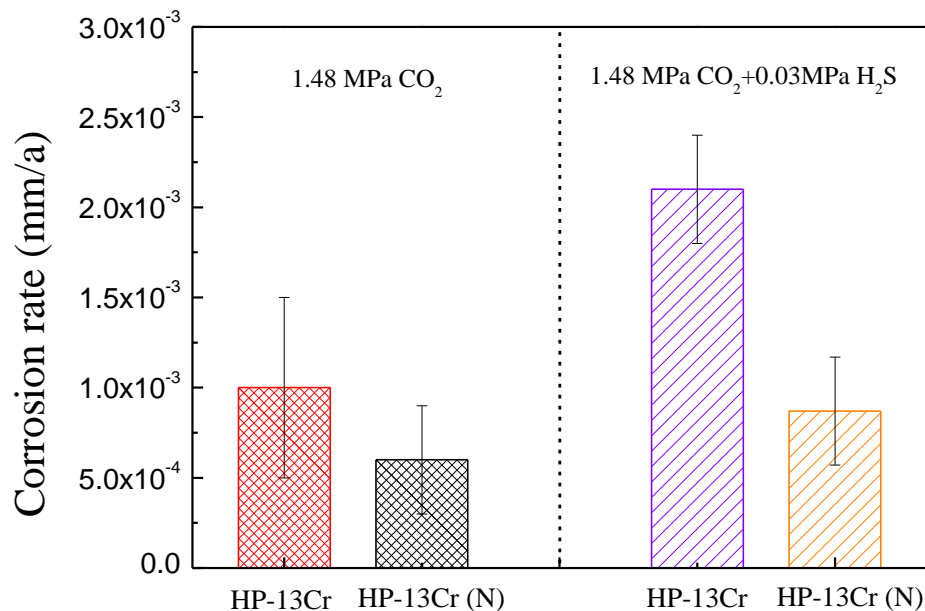


Figure 3. Corrosion rate of HP-13Cr SS and HP-13Cr(N)SS at CO₂ (1.48 MPa) and CO₂ (1.48 MPa)/H₂S (0.03 MPa) and 70 °C corrosion environment.

The Potentiodynamic polarization curves of HP-13Cr and HP-13Cr(N) at CO₂ corrosion environment are shown in Fig. 4. The open circuit potentials of HP-13Cr(N) and HP-13Cr are $-0.28 V_{SHE}$ and $-0.24 V_{SHE}$, respectively. The passivation current of HP-13Cr(N) is smaller than that of HP-13Cr in the partial passivation interval. The passivation current density of HP-13Cr is $3.36 \times 10^{-5} A/cm^2$, while the passivation current density of HP-13Cr(N) is $2.41 \times 10^{-5} A/cm^2$. The range of passivation interval is a critical indicator for corrosion resistance. Notably for each stainless steel, all the specimens showed obvious passivation characteristics. The corrosion potential decreased to $-0.28 V_{SHE}$ from $-0.24 V_{SHE}$ after adding nitrogen. However, the length of passivation interval of HP-13Cr(N) SS is about twice that of HP-13Cr SS in CO₂ corrosion environment. Notably, N addition in HP-13Cr stainless steel significantly broadened the passive region and decreased the corrosion potential at CO₂ corrosion environment. The results of electrochemical measurement are consistent with the results of corrosion rate shown in Fig. 3. In addition, this results are similar with our previous study[5] that the corrosion resistance of austenitic stainless steel in 3.5% NaCl solution has been improved after nitriding.

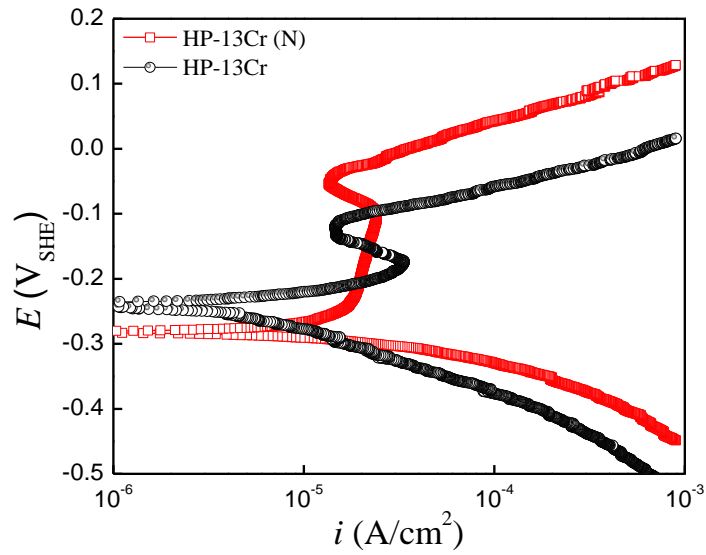


Figure 4. Potentiodynamic polarization curves of HP-13Cr SS and HP-13Cr (N) SS at CO₂ corrosion environment.

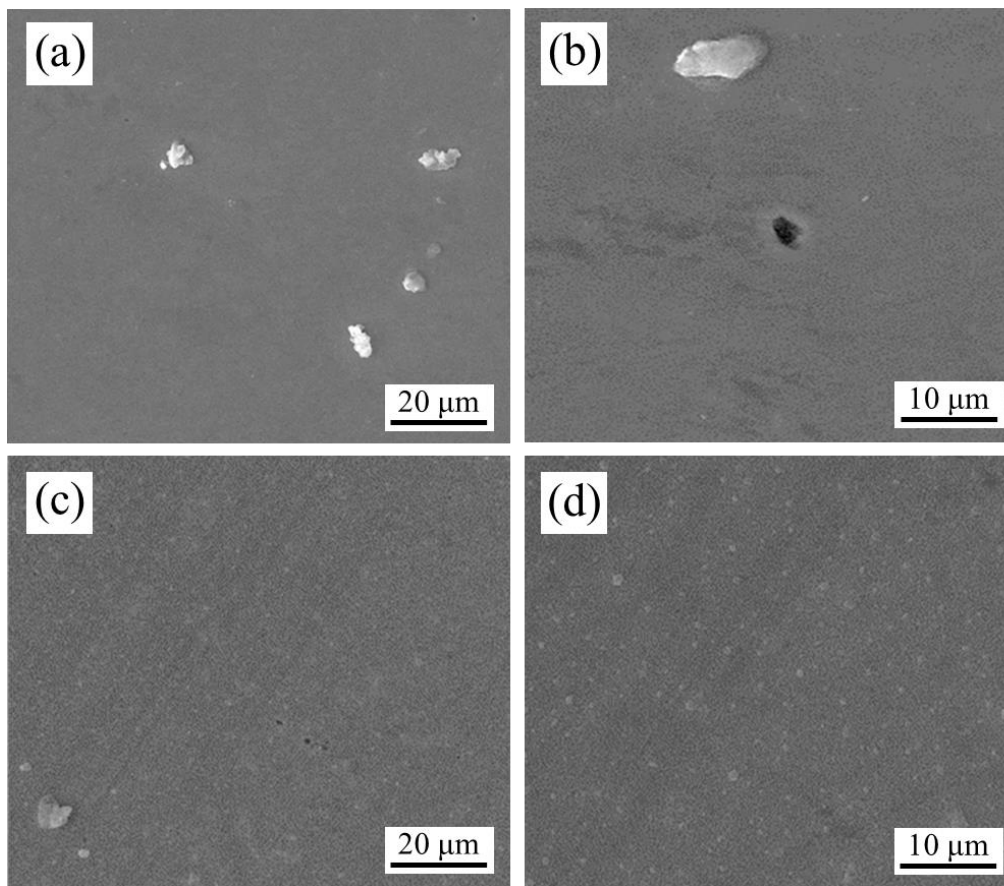


Figure 5. Surface morphology of corrosion scales of HP-13Cr SS and HP-13Cr (N) SS at CO₂ (1.48 MPa) corrosion environment. (a, b) HP-13Cr SS, (c, d) HP-13Cr (N) SS.

The surface corrosion morphologies of HP-13Cr SS and HP-13Cr (N) at CO₂ corrosion environment are shown in Fig. 5. Corrosion products appeared on the surface of HP-13Cr (Fig. 5a),

and corrosion pits were also observed (Fig. 5b). However, the HP-13Cr (N) surface is flat with several polishing marks remaining (Figs. 5c-d).

The surface corrosion morphologies of HP-13Cr SS and HP-13Cr (N) at CO₂/H₂S corrosion environment are shown in Fig. 6. The HP-13Cr surface become corroded and rough, indicating severe corrosion. The surface of HP-13Cr (N) is relatively flat, and the corrosion film is more compact. Compared with the Dai's study [5], both austenitic stainless steel and martensitic stainless steel with N added show better corrosion resistance.

The full XPS spectra of corrosion products of base steel and N-added steel at different corrosion environments are shown in Fig. 7. The corrosion products contain Fe, Cr, O, and C. To evaluate the specific composition of compounds in corrosion products, the peak fitting for each element was performed using a computer software. The results of peak fitting are shown in Fig. 8.

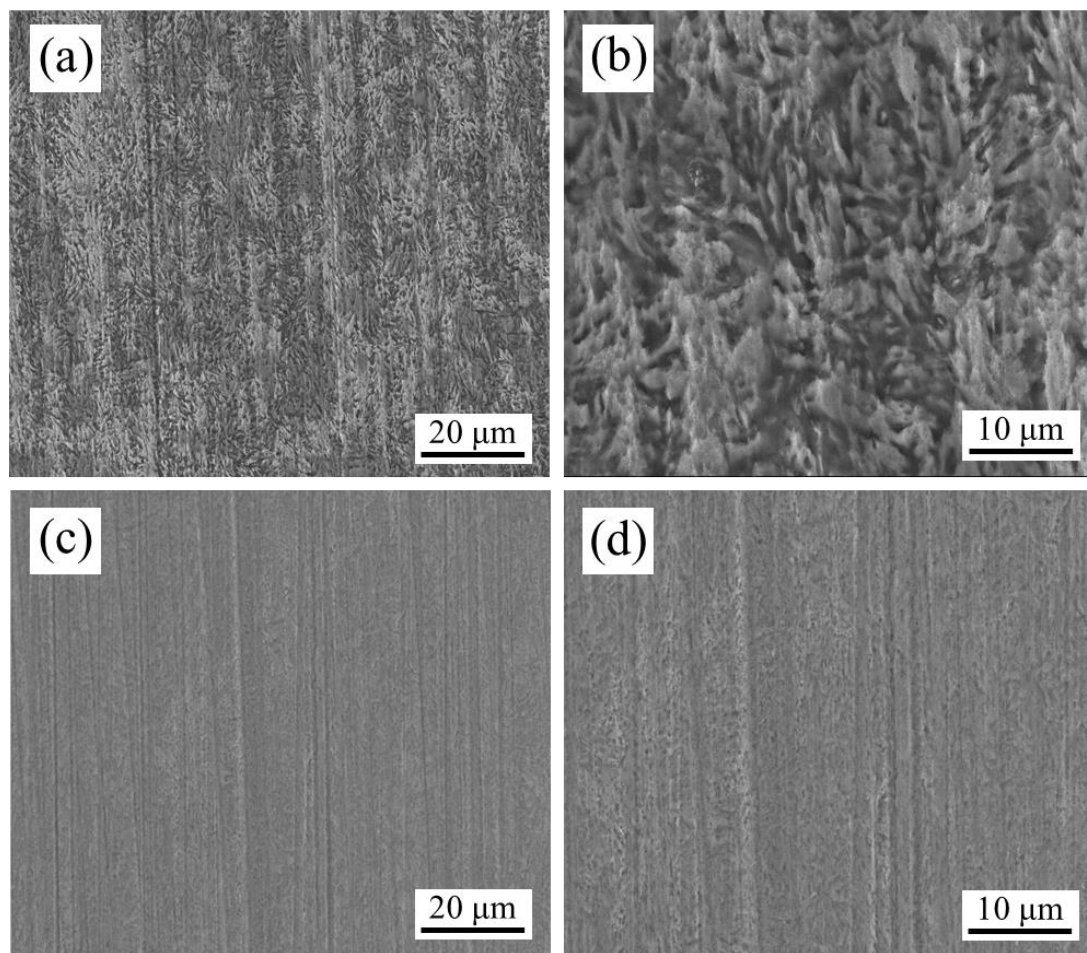


Figure 6. Surface morphology of corrosion scales of HP-13Cr SS and HP-13Cr (N) SS at CO₂ (1.48 MPa)/H₂S (0.03 MPa) corrosion environment. (a, b) HP-13Cr SS,(c, d) HP-13Cr (N) SS.

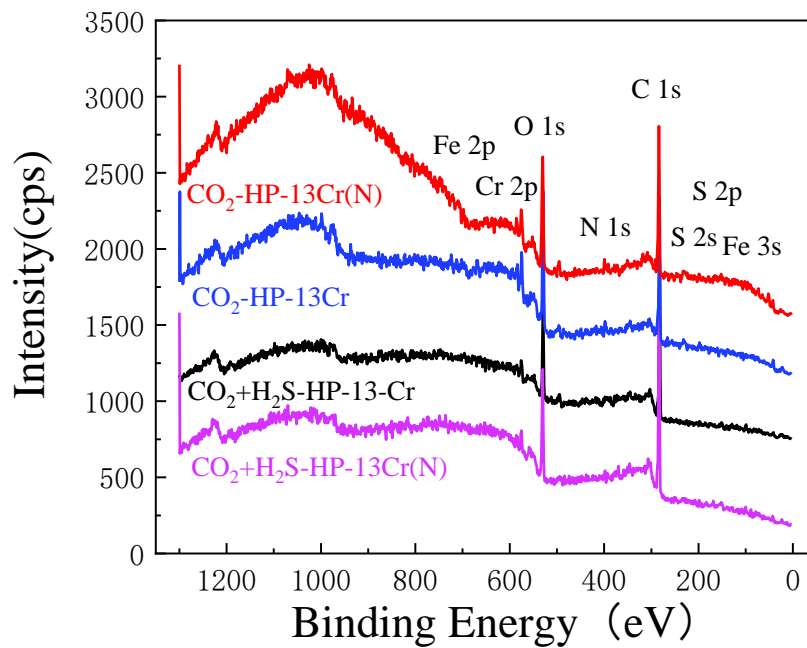
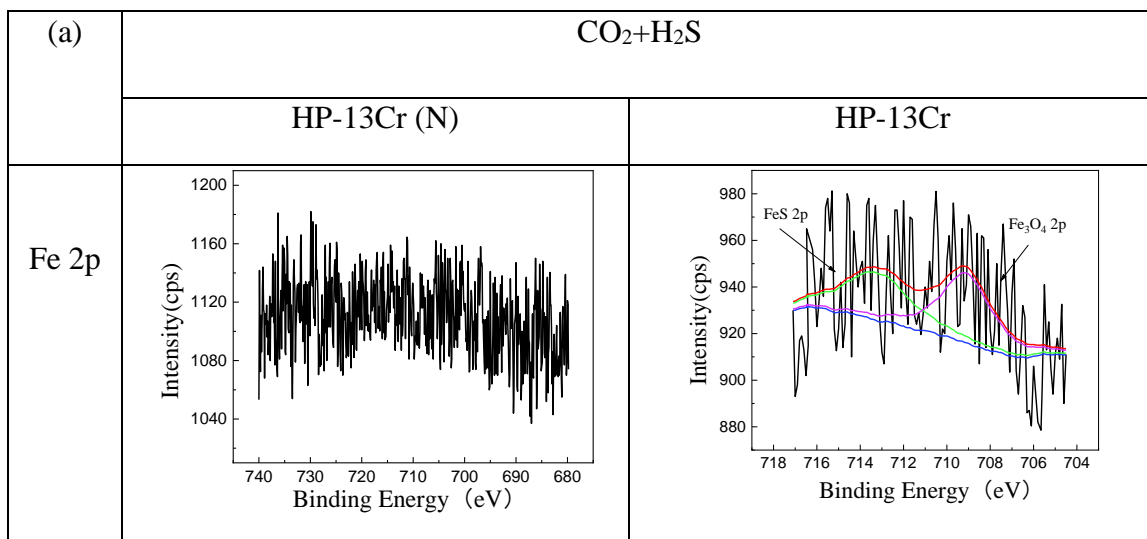
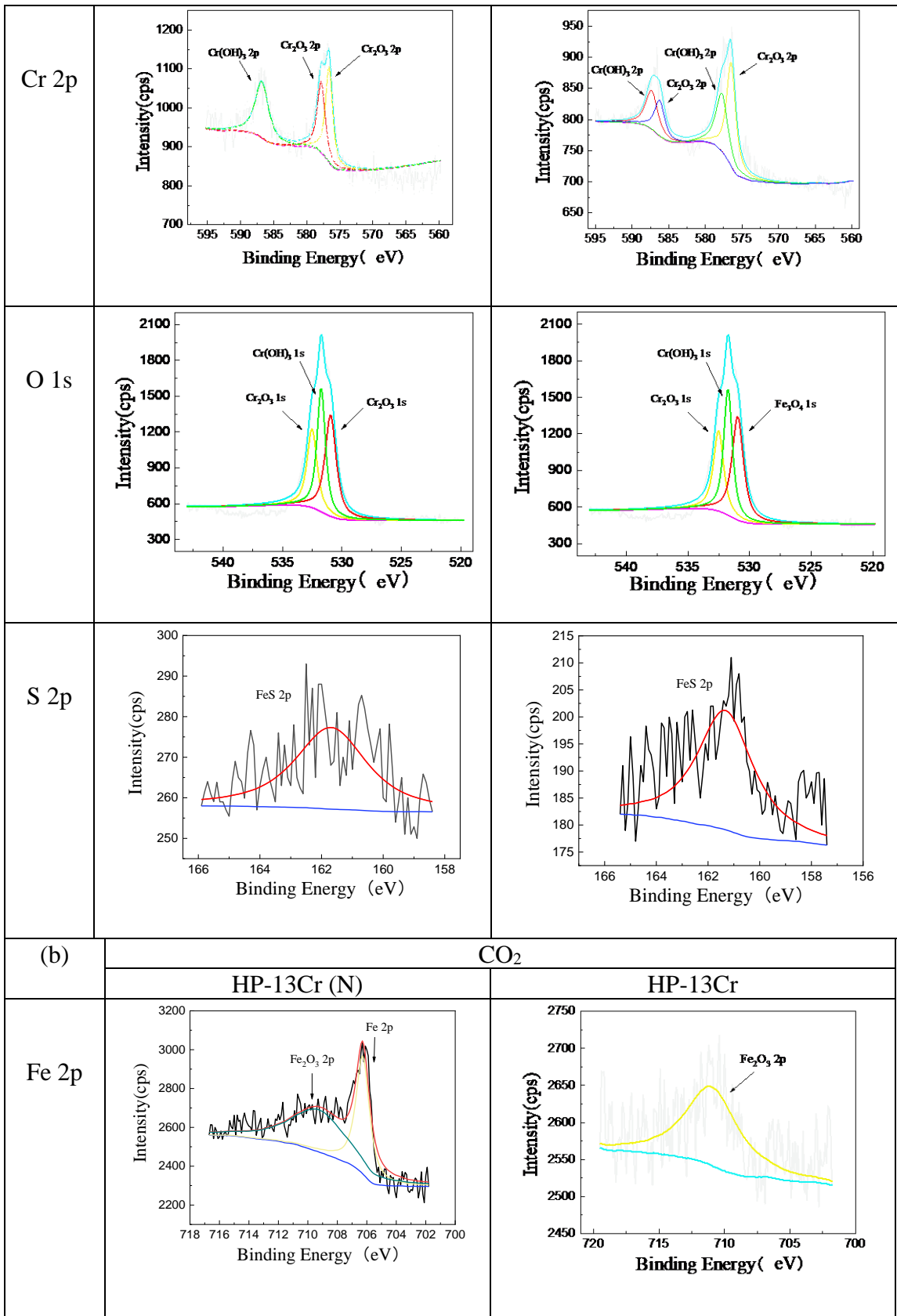


Figure 7. Full XPS spectra of corrosion products of HP-13Cr SS and HP-13Cr (N) SS at CO₂ (1.48 MPa) and CO₂ (1.48 MPa)/H₂S (0.03 MPa) corrosion environment.

When the corrosion environment is CO₂+H₂S, both HP-13Cr SS and HP-13Cr-0.28N SS generate Cr (OH)₃, Cr₂O₃, and FeS. The types of chromium compounds are similar to those in previous study [12] This phenomenon is also found in other martensitic steels in H₂S environment [34]. Ferrous sulfide has a harmful effect on the passivation film, consistent with the increase in the corrosion rate of N-added steel and base steel in CO₂/H₂S environment shown in Figure 3. However, Fe₃O₄ only exists in the surface of base steel. When the corrosion environment is CO₂, the corrosion products for two materials are the same.





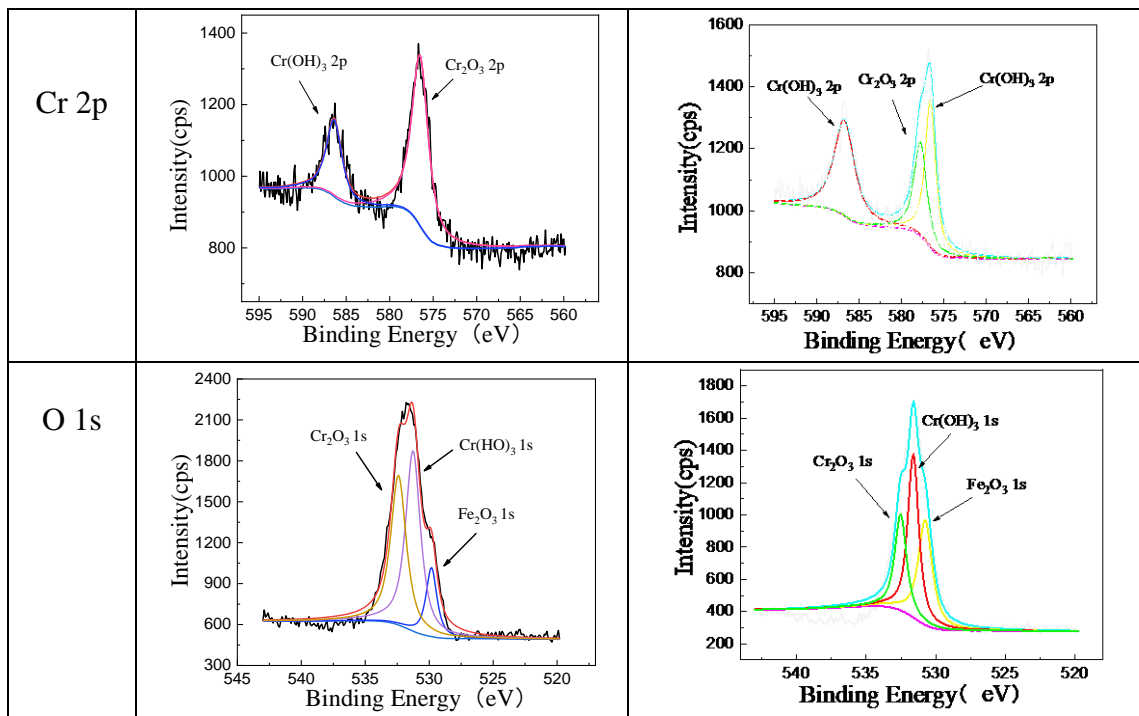


Figure 8. XPS results of each element at (a) CO₂ (1.48 MPa)/H₂S (0.03 MPa) corrosion environment and (b) CO₂ (1.48 MPa) corrosion environment.

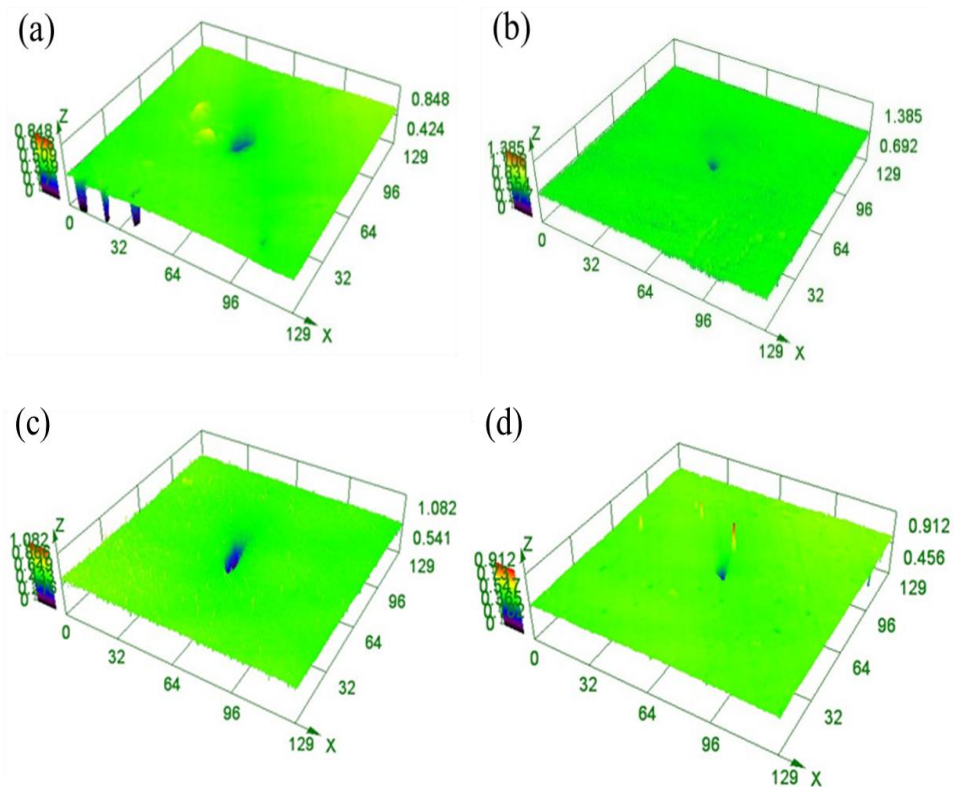


Figure 9. The 3D view of typical morphologies of maximum pits: (a) HP-13Cr at CO₂ (1.48 MPa) environment; (b) HP-13Cr (N) at CO₂ (1.48 MPa) environment; (c) HP-13Cr at CO₂ (1.48 MPa)/H₂S (0.03 MPa) environment; (d) HP-13Cr (N) at CO₂ (1.48 MPa)/H₂S (0.03 MPa) environment.

The 3D views of typical morphologies of maximum pits for two samples in different corrosion environments are shown in Fig. 9. As shown in Figs. 9(a, c), deep and wide pits are observed on the base steel surface at two corrosion environments due to pitting corrosion. After adding nitrogen, all the corrosion pits became smaller at two environments (Figs. 9b, d). This typical pits morphology of HP-13Cr also appeared in another previous study [13].

The cumulative probabilities of maximum depth and width of HP-13Cr SS and HP-13Cr (N) SS at (a-b)CO₂ and (c-d)CO₂/H₂S corrosion environments are shown in Figs. 10 (a-b) and (c-d), respectively. Zhao [13] also used this method in his research on HP-13Cr stainless steel in the extremely aggressive oilfield environment. As shown in Figs. (a-b), the maximum pitting depth decreased, while the maximum pitting width increased at CO₂ corrosion environment after adding nitrogen. However, both the maximum pitting depth and width of HP-13Cr (N) SS decreased at CO₂/H₂S corrosion environment (Figs. 10c-d).

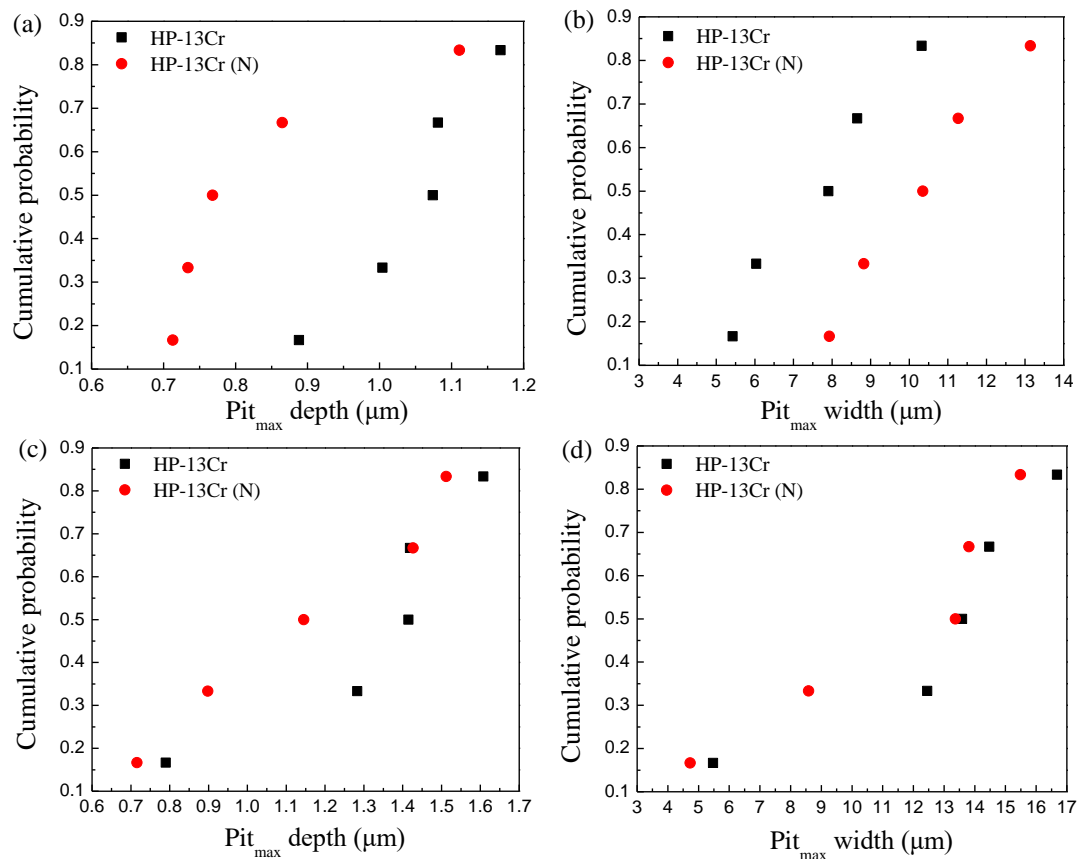


Figure 10. Cumulative probability of maximum depth and width of HP-13Cr SS and HP-13Cr (N) SS at (a, b) CO₂ (1.48 MPa) and (c, d) CO₂ (1.48 MPa)/H₂S (0.03 MPa) corrosion environment.

4. CONCLUSIONS

Both electrochemical and weight loss tests show that the addition of N improves the corrosion resistance of HP-13Cr stainless steel in a simulated extreme environment. The corrosion morphology

changes in the two steels in CO₂ and CO₂/H₂S environment are also consistent with the results of weight loss test. XPS analysis shows that the decrease in corrosion resistance of HP-13Cr stainless steel in a sulfur-containing environment can be attributed to the formation of ferrous sulfide which has a harmful effect on the passivation film. By adding nitrogen on the surface of HP-13Cr stainless steel, the nitrogen and chromium elements could form compounds, thus decreasing the corrosion rate of substrate. Therefore, in the oil and natural gas fields, the corrosion resistance of HP-13Cr in extremely aggressive environments can be improved by adding nitrogen.

References

1. J. Han, J. Zhang and J. W. Carey, *Int. J. Greenhouse Gas Control*, 5 (2011) 1680
2. J. He, L. Chen, Z. H. Guo, H. H. Zhi, S. Antonov and Y. J. Su, *Mater. Sci. Eng., A*, 793 (2020) 139835.
3. B. J. Dong, W. Liu, Y. Zhang, W. Banthukul, Y. G. Zhao, T. Y. Zhang, Y. M. Fan and X. G. Li, *J. Nat. Gas Sci. Eng.*, 80 (2020) 103371.
4. J. Mehdi, H. S. M. Saleh and S. M. Hossein, *Corros. Sci.*, 163 (2020) 108230.
5. J. Dai, H. Feng, H. B. Li, Z. H. Jiang, H. Li, S. C. Zhang, P. Zhou and T. Zhang, *Corros. Sci.*, 174 (2020) 108792.
6. J. X. Hou, W. W. Song, L. W. Lan and J. W. Qiao, *J. Mater. Sci. Technol.*, 48 (2020)140.
7. M. Bianco, S. Poitel, J. E. Hong, S. C. Yang, Z. J. Wang, M. Willinger, R. Steinberger-Wilckens and J. Van herle, *Corros. Sci.*, 165 (2020) 108414.
8. Z. Rui, D. O. Northwood and L. Cheng, *J. Mater. Res. Technol.*, 9 (2020) 2331.
9. Q. Yang, L. R. Zhao and P. Patnaik, *Surf. Coat. Technol.*, 375 (2019) 763.
10. T. Y. Zhang, J. S. Wu, L. Jin, Z. Zhang, W. Rong, B. W. Zhang, Y. Wang, Y. D. He, W. Liu and X. G. Li, *J. Mater. Sci. Technol.*, 35 (2019) 2630.
11. E. Ura-Bińczyk, A. Krawczyńska, R. Sitek and M. Lewandowska, *Surf. Coat. Technol.*, 375 (2019) 565.
12. X. P. Li, Y. Zhao, W. L. Qi, J. F. Xie, J. D. Wang, B. Liu, G. X. Zeng, T. Zhang and F. H. Wang, *Appl. Surf. Sci.*, 469 (2019) 146.
13. Y. Zhao, X. P. Li, C. Zhang, T. Zhang, J. F. Xie, G. X. Zeng, D. K. Xu and F. H. Wang, *Corros. Sci.*, 145 (2018) 307.
14. Q. C. Wang, B. C. Zhang, Y. B. Ren and K. Yang, *Corros. Sci.*, 145 (2018) 55.
15. F. Borgioli, E. Galvanetto and T. Bacci, *Corros. Sci.*, 136 (2018) 352.
16. Y.D. Zhu, M. F. Yan, Y. X. Zhang, H. T. Chen and Y. Yang, *Vacuum.*, 134 (2016) 25.
17. S.A. Saadi, Y. S. Yi, P. Y. Cho, C. H. Jang and P. Beeley, *Corros. Sci.*, 111 (2016) 720.
18. M. Gholami, M. Hoseinpoor and M. H. Moayed, *Corros. Sci.*, 94 (2015) 156.
19. R. K. Gupta and N. Birbilis, *Corros. Sci.*, 92 (2015) 1.
20. I. Pohrelyuk, O. Tkachuk and R. Proskurnyak, *Cent. Eur. J. Chem.*, 12 (2014) 260.
21. H. Wang and J. A. Turner, *Fuel Cells Bull.*, 13 (2013) 917.
22. H.T. Wang and E. H. Han, *Electrochim. Acta*, 90 (2013) 128.
23. A. Martinavičius, G. Abrasonis, A. C. Scheinost, R. Danoix, F. Danoix, J. C. Stinville, G. Talut, C. Templier, O. Liedke, S. Gemming and W. Möller, *Acta Mater.*, 60 (2012) 4065.
24. T. Watanabe, M. Kondo and A. Sagara, *Electrochim. Acta.*, 58 (2011) 681.
25. F.Z. Bouanis, C. Jama, M. Traisnel and F. Bentiss, *Corros. Sci.*, 52 (2010) 3180.
26. P. Marcus, V. Maurice and H.H. Strehblow, *Corros. Sci.*, 50 (2008) 2698.
27. Z.L. Li, J.H. Shang, W. Liu and B. Fei, *Surf. Coat. Technol.*, 202 (2008) 4830.
28. M. Kuczynska-Wydorska and J. Flis, *Corros. Sci.*, 50 (2007) 523.
29. Z.L. Li, J.C. Qi and W. Liu, *Metall. Mater. Trans. A.*, 37 (2006) 439.

30. D.D. Macdonald, A.C. Scott, P. Wentrccek, *J.Electrochem. Soc.*, 126 (1979) 908.
31. J.Z. Wang, J.Q. Wang, H.L. Ming, Z.M. Zhang, E.H. Han, *Mater. Sci. Technol.*, 34 (2018) 1419.
32. E. Barnatov, T. Hughes, J. Geddes, M. Nagl, Research on Corrosion Inhibitors for Acid Stimulation, NACE, 2012, C2012-0001573.
33. H.Y. Shen, L. Wang and J.C.Sun , *Surf. Coat. Technol.*, 385 (2020) 125450
34. X.W. Lei, H.Y. Wang, F.X. Mao, J.P. Zhang, M.F. Zhao, A.Q. Fu, Y.R. Feng and D.D. Macdonald, *Corros. Sci.*, 131 (2018) 164

© 2021 The Authors. Published by ESG (www.electrochemsci.org). This article is an open access article distributed under the terms and conditions of the Creative Commons Attribution license (<http://creativecommons.org/licenses/by/4.0/>).